Check for updates

Solar RRL

www.solar-rrl.com

Dielectric Bragg Reflector as Back Electrode for Semi-Transparent Organic Solar Cells with an Average Visible Transparency of 52%

*Leonie Pap, Bertolt Schirmacher, Esther Bloch, Clemens Baretzky, Birger Zimmermann, and Uli Würfel**

A crucial challenge in the development of semi-transparent solar cells is to maintain a reasonable power conversion efficiency (PCE) while reaching a high average visible transparency (AVT). Typically, organic semiconductors are favorable for this application since they can selectively absorb infrared light while transmitting visible light. This ability stems from limited electronic states at high(er) energies in contrast to inorganic semiconductors with their typical rise of the absorption coefficient toward higher photon energies. To increase PCE at high AVTs, a series of infrared dielectric Bragg reflectors is developed for semi-transparent organic solar cells. Using the multi-layered back electrode (TiO_2|SiN|TiO_2|AZO|Ag|AZO) with PV-X Plus as photoactive layer and a metal-free PEDOT:PSS top electrode, a light utilization efficiency (LUE = AVT × PCE) of up to 4.32% is achieved, together with an AVT of 47.9%. Although the short circuit current and AVT agree well with optical simulations, a low fill factor (FF) and partial shunting limit the overall device performance. Using ZnO and PFN-Br as additional electron transport layers and modifying the back electrode stack (TiO_2|SiO_2|TiO_2|AZO|Ag|AZO) accordingly leads to an LUE of up to 4.6% with a remarkable AVT of 51.9% and a maximum PCE of 8.79%.

1. Introduction

Amidst the effort for climate protection and decreasing CO_2 emissions, solar cells offer a viable solution for renewable energy generation. Renewable energy capacity increased by 50% in 2023 to nearly 510 GW globally, with solar PV accounting for three-quarters of new installations worldwide, as per the latest IEA report, Renewables 2023.[1] This comes as no surprise as solar energy is widely regarded as one of the top contenders for meeting humanity's energy demands.[2,3] Still, a significant challenge is to allocate appropriate land for photovoltaic installations, particularly in densely populated regions, where they compete with agriculture, face stringent zoning regulations, and must strike a balance between environmental considerations and the push for more renewable energy.[4] Integrating compatible renewable technologies into urban and agricultural environments is therefore of increasing importance to meet demand sustainably and optimize the utilization of land simultaneously.[5–7] Due to this, the concept of building-integrated photovoltaics gained traction. Installing semi-transparent photovoltaics as power-generating windows, facades and greenhouses emerged as a promising development.[8–12] Semi-transparent solar cells (STSCs) maintain a high transmission in the visible region while utilizing the infrared region (and/or UV region) for energy conversion. Therefore, they are able to provide sustainable powergeneration without significantly impeding plant photosynthesis or human visibility. When developing STSCs, adjusting the material choice for the photoabsorber to the respective application (for instance selective absorption in the near-infrared[13,14] or ultraviolet[15,16] light regime for adjusted optical properties) is of utmost importance. Organic solar cells provide properties like mechanical flexibility, solution processability at low temperatures, and light-weightness that are beneficial for the production and installation of STSCs.[8,17–19] Additionally, by tailoring their molecular structure they have the ability to selectively absorb light in a spectral regime of choice.[10,20–22] This is due to their absorption coefficient, which – unlike inorganic semiconductors – does not rise continuously for higher photon energies.[23]

To compare and characterize both the visible transmission and power conversion efficiency (PCE) of such semi-transparent solar cells, multiple figures of merit are commonly used. Similarly to opaque solar cells, the PCE is used to compare device performance. The transmission received by the human eye is defined by the average visible transmission (AVT) based on the AM1.5G spectrum, the transmission of the device and the photopic response of the human eye.[8] Depending on the specific application an AVT of 25% is usually regarded as a minimal requirement for power-generating windows, although in recent years AVTs of over 50% have been set as a new standard.[24,25]

L. Pap, B. Schirmacher, E. Bloch, C. Baretzky, B. Zimmermann, U. Würfel
Fraunhofer Institute for Solar Energy Systems ISE
Heidenhofstr. 2, 79110 Freiburg, Germany
E-mail: uli.wuerfel@ise.fraunhofer.de

L. Pap, C. Baretzky, U. Würfel
Freiburg Material Research Center FMF
University of Freiburg
Stefan-Meier-Str. 21, 79104 Freiburg im Breisgau, Germany

The ORCID identification number(s) for the author(s) of this article can be found under https://doi.org/10.1002/solr.202400399.

DOI: 10.1002/solr.202400399

One of the most crucial challenges when developing semi-transparent organic solar cells (STOSCs) is to maintain a reasonable PCE while attaining high AVTs.[26,27] Typically, the PCE decreases with increasing AVT, since most organic semiconductors do not absorb exclusively outside the visible region. To identify the best trade-off between AVT and PCE, another figure of merit has been introduced: light utilization efficiency (LUE = AVT × PCE). Advanced device stack engineering, changes in active layer morphology, and combining new donor and acceptor materials are just a few examples of the efforts in research that led to the current state-of-the-art STOSCs. One example for achieving an outstanding AVT of 50.05% while also maintaining a high PCE of 10.01% was published by Zhang et al.[28] They reported an LUE of 5.01% by using sequential deposition of PCE10-2F and Y6 to achieve a favourable morphology, enhancing interfacial contact and charge dynamics while suppressing energy losses. In the regime of using complex device stack engineering to achieve high AVTs with good PCEs, Li et al. reported a PCE of 10.8% with an AVT of 45.7%.[29] Due to an additional anti-reflection-coating comprising MgF_2 and SiO_2 as well as an optical outcoupling layer stack of alternating MgF_2 and 4,4′-Bis(*N*-carbazolyl)-1,1′- biphenyl layers they were able to reach an LUE of 5.0%. Alternative engineering approaches include Liu et al. publishing a PCE of 11.43% with an AVT of 46.79% and an LUE of 5.35% for a solar cell stack with PM6: BTP-eC9: L8-BO as absorber.[30] The fabricated cell included a new transparent electrode stack incorporating a thermally evaporated aperiodic bandpass filter of lithium fluoride (LiF)|tellurium dioxide|LiF. Despite these promising developments, literature reports become more sparse when looking for AVTs of 50% and higher without PCEs dropping below 6%. In this work, we propose a series of dielectric Bragg reflectors as infrared-reflecting back electrodes consisting of an AZO|Ag|AZO stack (AZO: Aluminum doped ZnO) supported by different compositions of layers with an optical function only (including SiO_2, TiO_2, SiN, AZO, and Ag). Combined with the photoactive material PV-X plus as well as a combination of two different poly(3,4-ethylenedioxythiophene) (PEDOT:PSS) formulations as metal-free top electrode an AVT of 47.9% was achieved with a PCE of 8.48%. However, the cell performance and especially the yield were limited by shunting. Therefore, a series of experiments and optical simulations were carried out and led to an optimized, much more shunt-proof cell stack including ZnO as an additional electron transport layer. This enabled an improved AVT of around 52%. Simultaneously, the median PCE was increased to 8.56% (champion device 8.79%). Although the total LUE of ≈4.5% (champion device 4.6%) is somewhat lower than the reported state-of-the-art in literature, the results stand out due to their high AVT. Additionally, the engineering of the device stack was performed without an overall decrease in PCE despite using the same active layer material. This proves that optical simulations and the subsequent optimization of the layer stack are powerful tools to overcome the trade-off between PCE and AVT.

2. Results and Discussion

To reach an improved trade-off between AVT and PCE, the incorporation of a multilayer stack comprising silver and aluminum-doped zinc oxide (AZO) as an infrared-reflecting back electrode has demonstrated to be beneficial as reported in our recent work.[31] There we could successfully fabricate solar cells with an LUE of 4.0% by employing a single silver back electrode (AZO|Ag|AZO) in conjunction with a PV-X Plus photoactive layer and a highly conductive poly(3,4-ethylenedioxythiophene) (PEDOT:PSS) top electrode. Despite these advancements, an optimized infrared reflection remains an area for further improvement. Utilizing the SCOUT/CODE simulation software from W. Theiss, our analysis revealed that increasing the number of alternating AZO and silver layers in the back electrode enhances the steepness and the magnitude of the infrared reflection onset. To keep production costs minimal and avoid a strong reduction in AVT associated with additional silver layers, the improved electrode stack was augmented with only one additional AZO and silver layer. For this "double silver" electrode configuration (AZO|Ag|AZO|Ag|AZO), optical simulations were conducted to optimize the thickness of each layer, enhancing infrared reflection. The optimized layer stack (52 nm|14 nm|75 nm|13 nm|30 nm) exhibits a three-fold increase in the slope of the reflection between 600 and 750 nm, while the total reflection at 800 nm is doubled compared to the single silver electrode (45 nm|14 nm|40 nm). Additionally, the simulated spectra for reflection, transmission, and absorption of the double silver electrode show excellent agreement with the experimentally measured ones as can be seen in **Figure 1**.

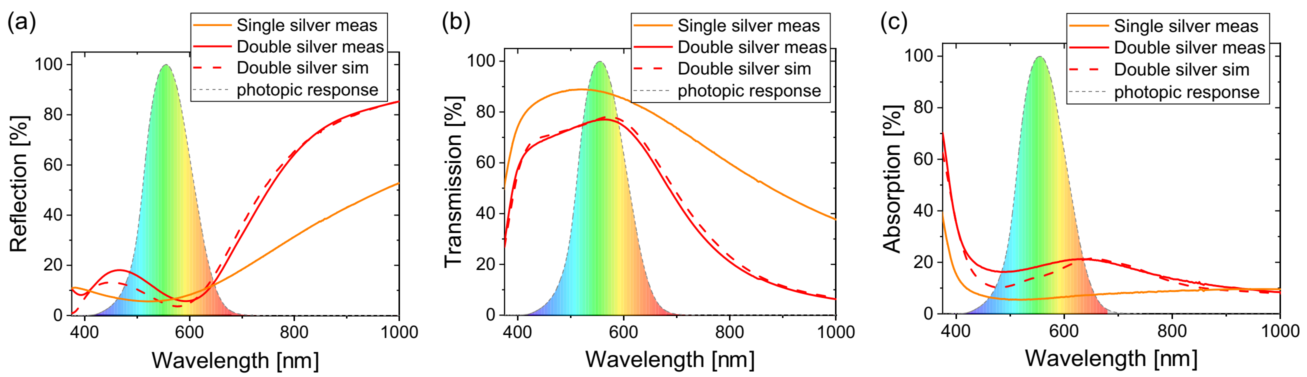

Figure 1. Simulated (dashed lines) and measured (solid lines) a) reflection, b) transmission and c) absorption spectra of the double silver electrode in comparison to the respective single silver electrode. Also shown is the photopic response of the human eye.

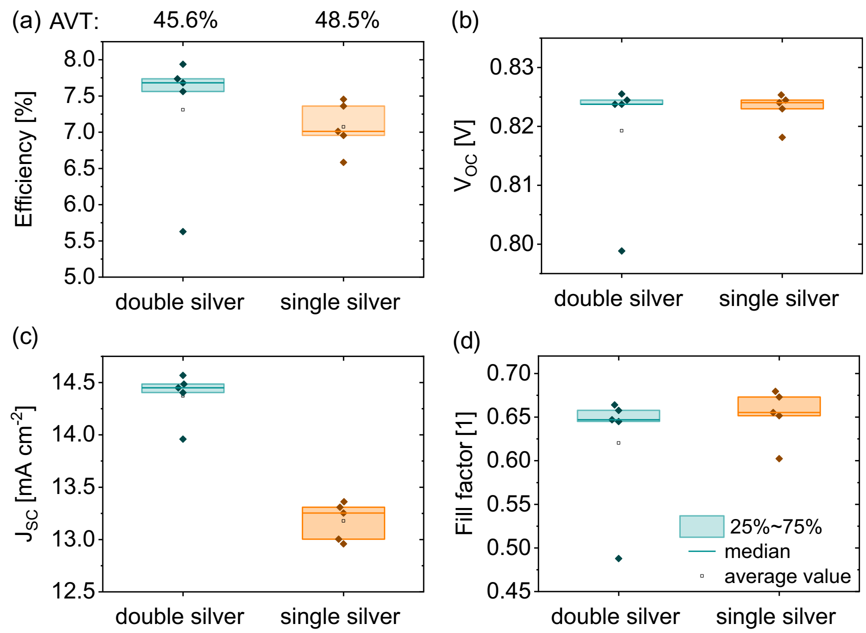

Figure 2. a) Efficiency and AVT, b) V_{OC}, c) J_{SC} and d) Fill Factor of solar cells with the double silver electrode compared to the single silver electrode (Glass| double or single silver electrode| PV-X Plus|hole transport layer and top electrode).

Subsequent experiments were conducted to compare the solar cell performance of the double silver electrode with the previously reported single silver electrode (**Figure 2**). An increase in short-circuit current density (J_{SC}) was observed for the cells with the double silver electrode, rising from 13.2 to 14.4 mA cm^{-2}, consistent with the simulated J_{SC} data (14.0 and 15.0 mA cm^{-2}, respectively).

Both the FF and open-circuit voltage (V_{OC}) remained comparable between the two configurations. However, the overall efficiency of the cells with the double silver electrode was higher than that of the single silver electrode, with median efficiencies of 7.68% and 7.01%, respectively. Despite the improvement in efficiency, the AVT values decreased significantly from 48.5% for single silver to 45.6% for double silver due to parasitic absorption of the additional silver layer in the visible.

To achieve higher AVTs while maintaining efficiency at a similar level, absorption in the back electrode must be minimized while maximizing infrared reflection at the same time. To do so, materials with suitable optical properties are used as an extension to the single silver electrode stack. A key principle underpinning this approach is the reflection that occurs at the interface of two materials with differing refractive indices. This phenomenon is described by Fresnel's equations, which provide a mathematical framework for understanding how light behaves at the boundary between two media. The reflection coefficient R at normal incidence is given by

$$R = \left| \frac{n_1 - n_2}{n_1 + n_2} \right|^2 \tag{1}$$

where n_1 and n_2 are the refractive indices of the two materials. This equation illustrates that a larger difference in refractive indices results in higher reflection at the interface. The materials chosen for the optical extension must therefore exhibit a minimal absorption coefficient, as well as substantial differences in their refractive indices, to maximize reflective properties and enhance reflectivity in the desired spectral ranges. Herein, two electrode extensions are proposed (**Figure 3**). One incorporates alternating layers of TiO_2 and SiN while the other uses thicker layers of TiO_2 and SiO_2. Specific layer thicknesses can be found in **Table 1**.

Optical simulations show an increase in reflection (at 800 nm) by 20% (the extension with the SiN interlayer) and 38.5% (for the extension with the SiO_2 interlayer) compared to the single silver electrode (Figure 3b). Additionally, the slope of the reflection onset (600–750 nm) doubles when using the extension incorporating SiN, and quadruples with the SiO_2 extended stack. Despite this increase in infrared reflection, we demonstrate that transmission (Figure 3c) and absorption (Figure 3d) in the visible region stay within a comparable range for all three configurations. To validate the accuracy of the optical simulations, measured and simulated reflection, transmission and absorption data of the extended electrode stacks were compared. The simulated spectra show excellent agreement with the measured data, confirming the reliability of the simulations. Experimental results for the corresponding cell performances can be seen in **Table 2**.

It may be noted, that for the cell with the extended SiN electrode different photoactive layer thicknesses lead to comparable LUE values, by exchanging PCE for AVT. The best cell performance, reaching an LUE of 4.32%, was achieved using a photoactive layer thickness of only 60 nm together with the extended electrode including the SiN interlayer. Surprisingly, the cells including the electrode with SiO_2 have the lowest median PCE, despite the promising simulation results. This can be attributed to the low FF of 50% which stems from shunting limitations shown in **Figure 4**a.

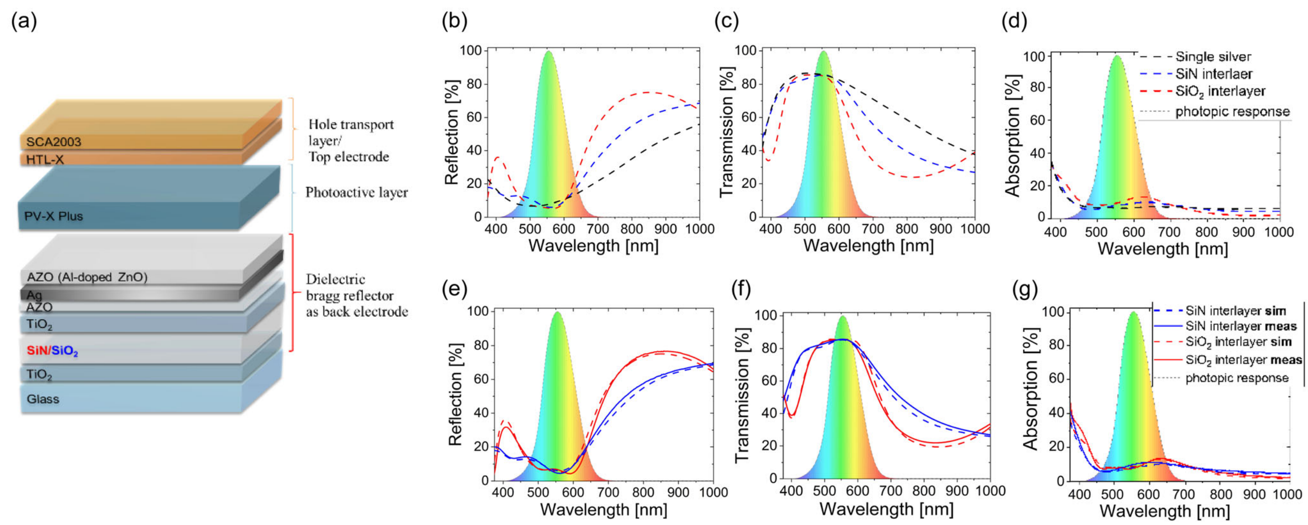

Figure 3. a) Schematic cell architecture with extended back electrode using a SiN or SiO_2 interlayer, respectively (specific layer thicknesses can be found in Table 1). b) Simulated reflection, c) transmission, and d) absorption spectra of the single silver reference cell (black) compared to the extended back electrode stacks. Simulated and measured e) reflection, f) transmission, and g) absorption spectra of the extended back electrode stacks.

Table 1. Specific layer thicknesses for the respective electrode stacks.

Electrode	Layers						
Single silver	Glass				AZO	Ag	AZO
	1100 nm				45 nm	14 nm	40 nm
Double silver	Glass	AZO	Ag		AZO	Ag	AZO
	1.1 mm	52 nm	14 nm		75 nm	13 nm	30 nm
DBR with SiO_2	Glass	TiO_2	SiO_2	TiO_2	AZO	Ag	AZO
No added ETL	1.1 mm	100 nm	113 nm	126 nm	5 nm	14 nm	38 nm
With added ETL	1.1 mm	103 nm	109 nm	125 nm	5 nm	14 nm	29 nm
DBR with SiN	Glass	TiO_2	SiN	TiO_2	AZO	Ag	AZO
	1.1 mm	55 nm	64 nm	22 nm	5 nm	14 nm	36 nm

In order to prevent these limitations, a 30 nm ZnO layer and a 5 nm PFN-Br layer were included as additional electron transport layers (ETLs) on top of the electrode stack. Using these additional ETL layers, no shunting effects were observed for the cells (Figure 4a). However, this comes at a cost of the J_{SC}. Since the cell performance is optically configurated for an architecture without the extra ETL layers, the alignment is shifted and with this, the photogenerated current decreases. Thus, in the next step, optical simulations were performed, now including the additional ETL layers. Both the uppermost AZO and the ZnO layer thicknesses were varied in order to find the best optical alignment and thus to reach the best theoretical LUE (Figure 4c). Since only photogenerated current and AVT can be simulated, but not V_{OC} and FF, the experimental median values for FF and V_{OC} for devices without additional ETL (0.5 and 0.83 V) were used to approximate the resulting LUE which is therefore quite low. Results show that the best LUE is achieved with a AZO layer thickness of 40 nm and an ZnO layer thickness of 0 nm. However, since the increase in FF when using additional ETL needs to be accounted for, the FF values with ZnO were adjusted (Figure 4d). As cells with additional ETL showed an improved average FF of 0.7, the FF was implemented in the simulated LUE data (Figure 4d) as follows: From 0 to 16 nm the FF is set to increase linearly from 0.5 to 0.7. For thicker ZnO layers, the FF is kept constant at 0.7. The latter was chosen since we observed saturation of the FF for thicknesses beyond about 16 nm. This comes as no surprise as the additional ETL shall predominately prevent micro-shunts and if this is achieved, no further improvement is to be expected for even thicker ZnO layers. Additionally, minor optical layer thickness variations were included to improve the overall alignment even more. With these adjustments, the best result was found for an AZO layer thickness of 29 nm and a ZnO layer thickness of 16 nm.

Lastly, experimental results of the respective cells can be found in **Figure 5** and Table 2. The simulated full stack reflection,

Table 2. Experimental results for cells with three different electrode configurations. Shown are the median values and the standard deviations of all working cells on a substrate including the best cell results in square brackets.

Electrode	Photoactive layer thickness [nm]	J_{SC} [mA cm^{-2}]	V_{OC} [V]	FF [1]	PCE [%]	AVT [%]	LUE [%]
Single silver	70 nm	15.65 (±0.11) [15.6]	0.83 (±0.004) [0.83]	0.63 (±0.04) [0.65]	8.17 (±0.53) [8.51]	45.6	3.73 (±0.24) [3.88]
SiN interlayer	70 nm	17.1 (±0.07) [17.1]	0.83 (±0.006) [0.83]	0.64 (±0.05) [0.66]	8.85 (±0.73) [9.36]	45.8	4.05 (±0.33) [4.29]
SiN interlayer	60 nm	15.5 (±1.92) [15.9]	0.83 (±0.004) [0.83]	0.66 (±0.06) [0.68]	8.48 (±1.41) [9.01]	47.9	4.06 (±0.67) [4.32]
SiO_2 interlayer	60 nm	15.45 (±0.05) [15.5]	0.81 (±0.013) [0.83]	0.50 (±0.08) [0.64]	6.20 (±1.17) [8.19]	49.0	3.05 (±0.57) [4.01]

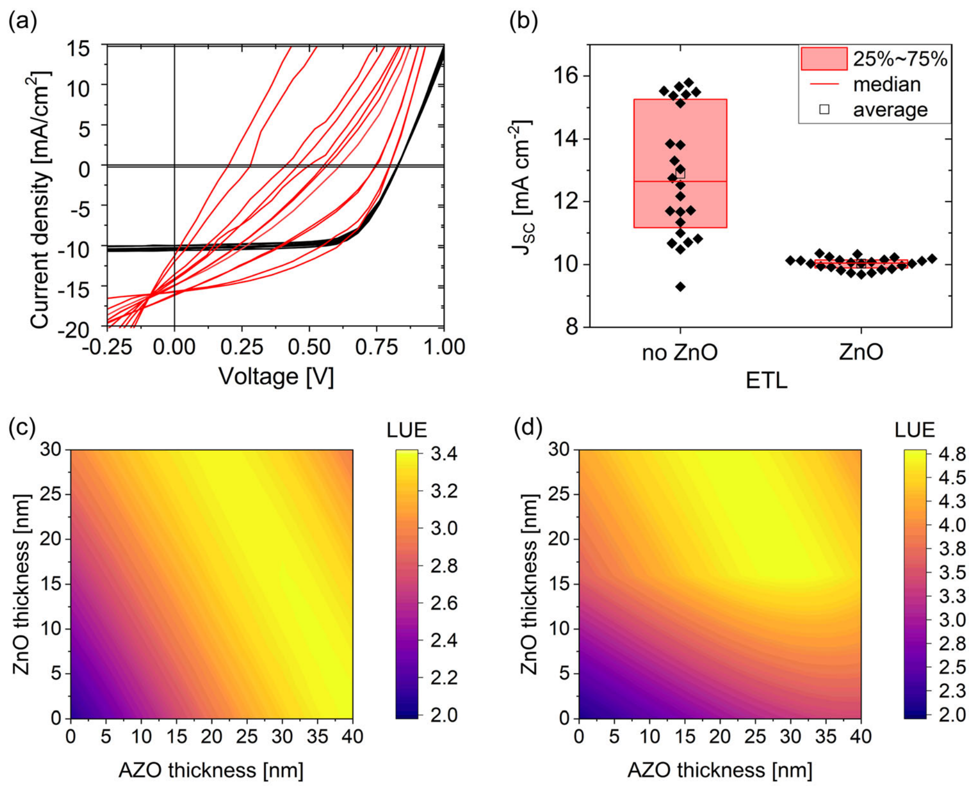

Figure 4. a) IV-curves for cells with the extended SiO_2 electrode with and without ZnO as electron transport layer and b) corresponding J_{SC} values. c) Estimated LUE values for cells with varying AZO and ZnO thicknesses (assuming a FF of 0.5 and V_{OC} 0.83 V). d) Simulation of the LUE with the V_{OC} set to 0.83 V and the FF increasing linearly from 0.5 for 0 nm ZnO to 0.7 for 16 nm after which it is kept constant.

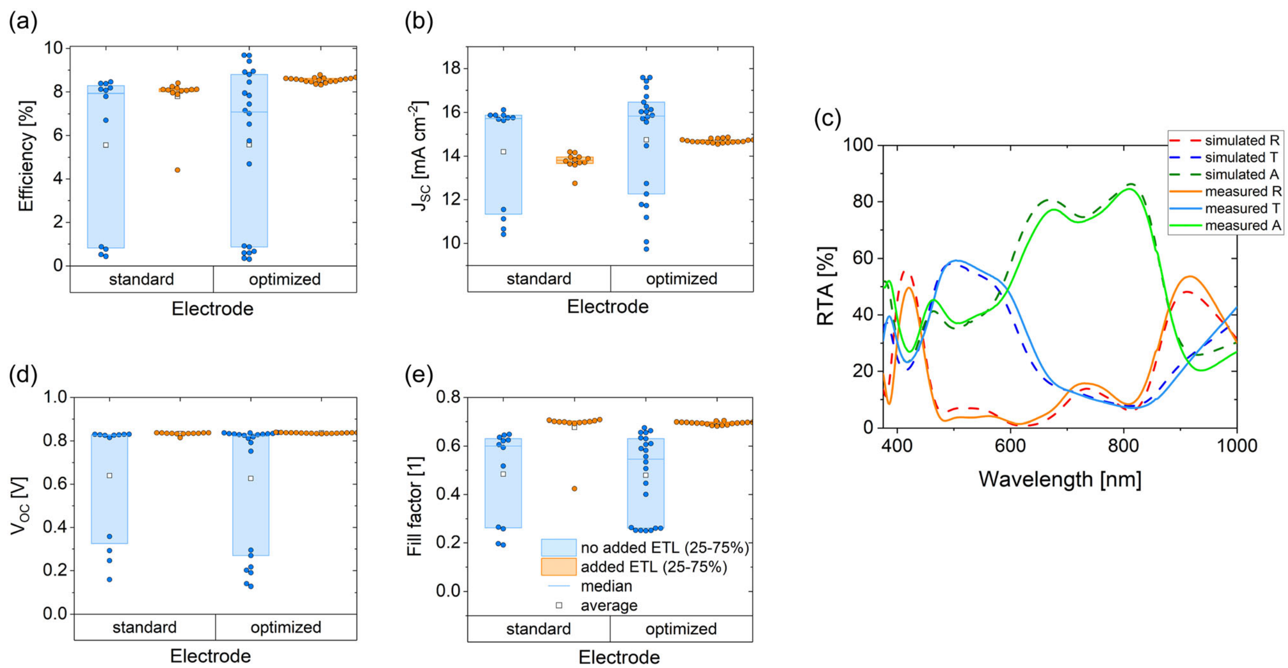

Figure 5. a) Efficiency, b) J_{SC}, d) V_{OC}, and e) FF of the electrode optically optimized for additional ETL layers compared to the previous version, both with and without additional ETL layers. c) Simulated and measured reflection, transmission, and absorption data of the optically optimized full stack.

Table 3. Experimental results for cells with standard and optimized electrode configurations with and without ZnO and PFN-Br as additional ETL layers. Shown are the median values of all working cells on a substrate including the standard deviation in brackets and the best cell results in square brackets for the overall highest LUE.

Electrode	ETL	J_{SC} [mA cm^{-2}]	V_{OC} [V]	FF [1]	PCE [%]	AVT [%]	LUE [%]
Standard	–	15.80 (±2.32) [15.7]	0.83 (±0.27) [0.83]	0.64 (±0.19) [0.65]	8.39 (±3.5) [8.46]	50.0	4.20 (±1.75) [4.23]
Standard	ZnO|PFN-Br	13.85 (±0.21) [14.2]	0.84 (±0.002) [0.84]	0.70 (±0.005) [0.71]	8.10 (±0.13) [8.41]	53.1	4.30 (±0.07) [4.47]
Optimized	–	15.85 (±2.46) [14.9]	0.83 (±0.28) [0.84]	0.62 (±0.17) [0.70]	8.20 (±3.59) [8.79]	48.5	4.00 (±1.74) [4.26]
Optimized	ZnO|PFN-Br	14.70 (±0.18) [14.90]	0.84 (±0.002) [0.84]	0.70 (±0.006) [0.70]	8.56 (±0.12) [8.79]	51.9	4.44 (±0.06) [4.56]

transmission and absorption data shows good agreement with the measured results (Figure 5c). Additionally, we demonstrate the improvements of the cell performance with the optimized cell stack. An increase in median FF of 10% can be observed when using ZnO and PFN-Br. The added ETL layers also provide a high reproducibility without any severe shunting. Although the median J_{SC} decreases for both the cells with the standard and with the optimized electrode design when adding ZnO and PFN-Br, we observe that the decrease for the cell with the optimized electrode is lessened. Overall, the median efficiency is highest when using the optimized cell stack including the added ETL layers, reaching a value of 8.65% with an AVT of 51.9%, giving an overall LUE of 4.44%. The champion device shows a PCE of 8.79% and thus an LUE of 4.56% (**Table 3**).

3. Conclusion

In this work, we demonstrate an enhanced AVT for organic solar cells utilizing PV-X Plus as an absorber and a multilayered dielectric Bragg reflector as an infrared-reflecting back electrode. Both optical simulations and experimental data are used to systematically improve the device stack. A double silver electrode configuration (AZO|Ag|AZO|Ag|AZO) significantly improves infrared reflection compared to a previously reported single silver electrode, tripling the slope of the reflection between 600 and 750 nm and doubling the total reflection at 800 nm. However, this enhancement results in a reduction of AVT from 48.5% to 45.6% due to parasitic absorption by the additional silver layer.

To achieve higher AVTs without a decrease in PCE, electrode extensions with materials exhibiting high refractive index contrasts and low absorption coefficients are investigated, such as TiO_2 combined with SiN or SiO_2. These configurations increase infrared reflection and thus PCE without compromising visible transmission. Experimental data for reflection, absorption, and transmission validate our optical simulation results. Incorporating additional electron transport layers (ETLs) like ZnO and PFN-Br mitigates shunting and reproducibility issues. Following optical optimization of the complete device, i.e., including ZnO and PFN-Br, the best performance is obtained with a (TiO_2|SiO_2|TiO_2|AZO|Ag|AZO) back electrode. A median efficiency of 8.56% is reached, comparable to previous stacks without ZnO and PFN-Br. Notably at the same time, AVT is increased to 51.9%, resulting in a median LUE of 4.44% with the best cell reaching an LUE of 4.56%. These results demonstrate how optical simulations and cell stack engineering can effectively increase AVT to clearly over 50% while maintaining similar PCE values.

4. Experimental Section

Device Fabrication and Characterization: In a first step in the fabrication of semi-transparent organic solar cells 25 × 25 mm^2 glass substrates purchased from Glasmanufaktur Pfähler were cleaned in ultrasonic baths of acetone, isopropanol and water for 10 min each and dry-blown with nitrogen. Alternating layers of TiO_2, SiO_2, SiN, AZO, and Ag were sputtered onto the glass substrates structured into active areas for six individual solar cells with a shadow mask.

A ZnO (N11 from Avantama diluted down to 1% nanoparticles in isopropanol) solution was spin-cast at RT and annealed for 10 min at 110 °C. Then PV-X Plus from Raynergy Tek (mixture of PV2300:PV-A-3:N1100 in a ratio of 1:1:0.2 with a concentration of 22 mg mL^{-1}) was spin-cast from o-xylene at 60 °C in a nitrogen-filled glove box (GB) and annealed for 10 min at 110 °C. A 40 nm HTL-X layer (purchased from Raynergy Tek) followed by 90 nm CLEVIOS^{TM} F HC SOLAR (R&D GRADE SCA 2003, supplied by Heraeus) was spin-cast (GB) on top of the photoactive layer and annealed for 2 and 5 min at 110 °C, respectively. Details regarding the CLEVIOS F HC SOLAR material can be found in our recent work.[31]

The HTL layers were structured by taping followed by a photoactive layer structuring by wiping with o-xylene. Lastly, a support structure of 4 nm Cr followed by 100 nm Ag was deposited via thermal evaporation at a pressure below 10^{-5} mbar outside, but closely around the active area.

Current–voltage measurements under simulated AM1.5G light by a class A solar simulator (Newport SP94063A-SR1-167, corrected for spectral mismatch) were carried out with a computer-programmed Keithley 2400 source meter.

UV/VIS measurements were carried out from 280 to 1200 nm by a Perkin Elmer Lambda 950 UV/Vis/NIR spectrophotometer. Layer thicknesses were determined with a Veeco Dektak 150 measuring samples of single layers on glass substrates.

Analysis: Optical modeling was conducted using the transfer matrix method with the software package CODE/SCOUT from W. Theiss. The optical coefficients, specifically the refractive index (n) and extinction coefficient (k), for all materials were derived using a Kim oscillator model. The model was fitted to measured reflection, absorption, and transmission data of single layers with specified thicknesses on glass substrates. These optical coefficients were then utilized to simulate the complete solar cell stack, with either defined or as a function of layer thicknesses to calculate theoretical current generation and AVT, taking optical interference effects into account. Through this approach, layer thickness optimization was performed using fit parameter settings to maximize both AVT and current generation.

AVT is used to characterize semi-transparent solar cells by incorporating the transmission of the solar cell stack $T(\lambda)$, the intensity of the solar AM1.5G spectrum $S(\lambda)$ and the photopic response of the human eye $P(\lambda)$. It is defined as follows[32]

$$\text{AVT} = \frac{\int T(\lambda)\, P(\lambda)\, S(\lambda)}{\int P(\lambda)\, S(\lambda)} \tag{2}$$

Acknowledgements

The authors acknowledge funding from the German Federal Ministry for Economic Affairs and Climate Protection (FKz. 03EE1119).

Conflict of Interest

The authors declare no conflict of interest.

Data Availability Statement

The data that support the findings of this study are available from the corresponding author upon reasonable request.

Keywords

device stack engineering, infrared mirror, light utilization efficiency, optical modeling, reflecting back electrode, semi-transparent organic solar cells

Received: May 29, 2024
Revised: June 14, 2024
Published online:

[1] IEA, Renewables 2023, https://www.iea.org/reports/renewables-2023 (accessed: April, 2024).
[2] Energy Institute, in *Statistical Review of World Energy*, **2023**, https://www.energyinst.org.statistical-review/home (accessed: April, 2024).
[3] A. J. C. Trappey, C. V. Trappey, H. Tan, P. H. Y. Liu, S.-J. Li, L.-C. Lin, *J. Cleaner Prod.* **2016**, *112*, 1709.
[4] I. Guaita-Pradas, I. Marques-Perez, A. Gallego, B. Segura, *Environ. Monit. Assess.* **2019**, *191*, 764.
[5] Z. Zhou, Z. Yuan, Z. Yin, Q. Xue, N. Li, F. Huang, *Green Energy Environ.* **2024**, *9*, 992.
[6] T. M. Koh, H. Wang, Y. F. Ng, A. Bruno, S. Mhaisalkar, N. Mathews, *Adv. Mater.* **2022**, *34*, e2104661.
[7] S. Chamara, C. Beneragama, *J. Sol. Energy Res.* **2020**, *5*, 417.
[8] Z. Hu, J. Wang, X. Ma, J. Gao, C. Xu, K. Yang, Z. Wang, J. Zhang, F. Zhang, *Nano Energy* **2020**, *78*, 105376.
[9] S. Han, Y. Deng, W. Han, G. Ren, Z. Song, C. Liu, W. Guo, *Sol. Energy* **2021**, *225*, 97.
[10] Y. Li, C. Ji, Y. Qu, X. Huang, S. Hou, C.-Z. Li, L.-S. Liao, L. J. Guo, S. R. Forrest, *Adv. Mater.* **2019**, *31*, e1903173.
[11] T. Jiang, G. Zhang, R. Xia, J. Huang, X. Li, M. Wang, H.-L. Yip, Y. Cao, *Mater. Today Energy* **2021**, *21*, 100807.
[12] D. Wang, H. Liu, Y. Li, G. Zhou, L. Zhan, H. Zhu, X. Lu, H. Z. Chen, C.-Z. Li, *Joule* **2021**, *5*, 945.
[13] J. Wang, J. Zhang, Y. Xiao, T. Xiao, R. Zhu, C. Yan, Y. Fu, G. Lu, X. Lu, S. R. Marder, X. Zhan, *J. Am. Chem. Soc.* **2018**, *140*, 9140.
[14] M. Bates, C. Malhado, C. Yang, C. K. Herrera, R. R. Lunt, *Sol. RRL* **2023**, *7*, 2200962.
[15] N. C. Davy, M. Sezen-Edmonds, J. Gao, X. Lin, A. Liu, N. Yao, A. Kahn, Y.-L. Loo, *Nat. Energy* **2017**, *2*, 849.
[16] X. Yan, J. Wang, W. He, T. A. Dela Peña, C. Zhu, H. Yu, Y. Hu, C. Yan, S. Ren, X. Chen, Z. Wang, J. Wu, M. Li, J. Xia, L. Meng, S. Lu, D. Zhao, M. Artemyev, Y. Li, P. Cheng, *J. Energy Chem.* **2024**, *96*, 351.
[17] J. Gao, W. Gao, X. Ma, Z. Hu, C. Xu, X. Wang, Q. An, C. Yang, X. Zhang, F. Zhang, *Energy Environ. Sci.* **2020**, *13*, 958.
[18] Z. Xiao, S. Yang, Z. Yang, J. Yang, H.-L. Yip, F. Zhang, F. He, T. Wang, J. Wang, Y. Yuan, H. Yang, M. Wang, L. Ding, *Adv. Mater.* **2019**, *31*, e1804790.
[19] M. Zhang, Z. Xiao, W. Gao, Q. Liu, K. Jin, W. Wang, Y. Mi, Q. An, X. Ma, X. Liu, C. Yang, L. Ding, F. Zhang, *Adv. Energy Mater.* **2018**, *8*, 1801968.
[20] J. Wang, P. Xue, Y. Jiang, Y. Huo, X. Zhan, *Nat. Rev. Chem.* **2022**, *6*, 614.
[21] Y. Li, Y. Zheng, C. Yan, J. Wang, P. Cheng, S. Zhang, *Sol. RRL* **2023**, *7*, 2300037.
[22] J. W. Yoon, H. Bae, J. Yang, J.-W. Ha, C. Lee, J. Lee, S. C. Yoon, H. Choi, S.-J. Ko, *Chem. Eng. J.* **2023**, *452*, 139423.
[23] H.-W. Cheng, Y. Zhao, Y. Yang, *Adv. Energy Mater.* **2022**, *12*, 2102908.
[24] M. B. Upama, M. Wright, N. K. Elumalai, M. A. Mahmud, D. Wang, K. H. Chan, C. Xu, F. Haque, A. Uddin, *Curr. Appl. Phys.* **2017**, *17*, 298.
[25] Q. Wei, Y. Zhang, T. Shan, H. Zhong, *J. Mater. Chem. C* **2022**, *10*, 5887.
[26] Y. Li, J. Wang, C. Yan, S. Zhang, N. Cui, Y. Liu, G. Li, P. Cheng, *Joule* **2024**, *8*, 527.
[27] H. Yu, J. Wang, Q. Zhou, J. Qin, Y. Wang, X. Lu, P. Cheng, *Chem. Soc. Rev.* **2023**, *52*, 4132.
[28] X. Huang, Y. Cheng, Y. Fang, L. Zhang, X. Hu, S. Y. Jeong, H. Zhang, H. Y. Woo, F. Wu, L. Chen, *Energy Environ. Sci.* **2022**, *15*, 4776.
[29] Y. Li, X. Guo, Z. Peng, B. Qu, H. Yan, H. Ade, M. Zhang, S. R. Forrest, *Proc. Natl. Acad. Sci. U. S. A.* **2020**, *117*, 21147.
[30] X. Liu, Z. Zhong, R. Zhu, J. Yu, G. Li, *Joule* **2022**, *6*, 1918.
[31] L. Pap, B. Schirmacher, E. Bloch, S. Bogati, P. Viehmann, A. Scheel, D. Müller, M. List, B. Zimmermann, U. Würfel, *Sol. RRL* **2023**, *7*, 2300561.
[32] C. Yang, D. Liu, M. Bates, M. C. Barr, R. R. Lunt, *Joule* **2019**, *3*, 1803.